Selective Four-Electron Reduction of Dioxygen by a Mononuclear Copper Complex Supported by a Pentadentate Polypyridylalkylamine Ligand

Mengqing Liu[a#], Yipei Zhao[a#], Qianyu Chang[a], Hongping Zhou[ab]*, Marcello Gennari[c]*, Carole Duboc[c]*, Lianke Wang[a]*

a. Institutes of Physical Science and Information Technology, Anhui University, Key Laboratory of Structure and Functional Regulation of Hybrid Materials (Ministry of Education), Anhui Province Key Laboratory of Chemistry for Inorganic/Organic Hybrid Functionalized Materials, Hefei, 230601, P. R. China. E-mail: wanglianke2009@163.com, zhzhp@263.net

b. School of Chemical and Environmental Engineering, Anhui Polytechnic University, Wuhu, 241000, P. R. China.

c. Département de Chimie Moléculaire, UMR 5250, Université Grenoble Alpes, 38000 Grenoble, France, E-mail: marcello.gennari@univ-grenoble-alpes.fr, carole.duboc@univ-grenoble-alpes.fr

1. Synthesis and characterization

1.1 General

1.1.1 Materials and instruments. N-(2-methylpyridine)-2,11-diaza[3.3](2,6)pyridinophane ligand was prepared as reported method.[1-2] All chemicals were purchased from commercial vendors and used as received. Tetrahydrofuran and diethyl ether were distilled over sodium and degassed prior to use. The synthesis and isolation were carried out under N_2 atmosphere by using glovebox or Schlenk technique. The ESI-MS spectra were registered on a Bruker Esquire 3000 Plus or Amazon speed ion trap spectrometer equipped with an electrospray ion source (ESI). The UV-Vis spectra were recorded on a Metash UV-8000 absorption spectrophotometer in quartz cells (optical path length: 1 cm).

Caution! Although we encountered no problem during preparation of complex, the perchlorate salts are potentially explosive and should be handled with caution.

***1.1.2 X-ray Crystallography*.** Single-crystal diffraction data was measured on a Bruker SMART APEX II CCD area detector diffractometer by using the graphite monochromated MoKa radiation (λ = 0.71073 Å) at 296 K, or on a XtaLAB Synergy R, HyPix diffractometer by using CuKα radiation (λ = 1.54178) at 120 K. SADABS-2014/5 (Bruker, 2014/5) was used for absorption correction. Subsequent steps were run under OLEX2[3]: the molecular structure was solved with SHELXT[4] structure solution program using Intrinsic Phasing and refined with the SHELXL[5] refinement package using Least Squares techniques. All non-hydrogen atoms were refined anisotropically. The hydrogen atoms were set geometrically and constrained to ride on their carrier atoms. CCDC 2500760, 2500761, 2500762, 2500763 contains the supplementary crystallographic data for this paper.

1.1.3 X-ray photoelectron spectroscopy. X-ray photoelectron spectroscopy (XPS) was conducted on a Thermofisher ESCALAB 250Xi spectrometer using a monochromatic Al-Kα source. The data were fitted by using the XPSPEAKS software.

1.1.4 Electron Paramagnetic Resonance. EPR spectra were recorded on a Bruker A300 X-band spectrometer.

EPR spectrum of $\mathbf{[Cu^{bmpa\text{-}NH}](ClO_4)_2}$ was recorded in acetonitrile (1.0 mM) at 77 K. microwave frequency = 9.4538 GHz, microwave power = 19.31 mW, modulation amplitude = 1 G, modulation frequency = 100 kHz, receiver gain = 2×10^2 , time constant = 1.25 ms, and conversion time = 180 ms.

EPR spectrum of $\mathbf{[Cu^{tmpa\text{-}NH}](ClO_4)_2}$ was recorded in acetonitrile (1.0 mM) at 77 K. microwave frequency = 9.4538 GHz, microwave power = 19.47 mW, modulation amplitude = 1 G, modulation frequency = 100 kHz,

receiver gain = 2× 10^2 , time constant = 1.25 ms, and conversion time = 120 ms.

1.2 Synthesis

1.2.1 synthesis of $[Cu^{tmpa\text{-}NH}](ClO_4)_2$

The pentadentate ligand N-(2-methylpyridine)-2,11-diaza[3.3](2,6)pyridinophane (20 mg, 0.06 mmol) was dissolved in mixture of methanol (1 mL) and acetonitrile (1 mL) in a vial, a $Cu(ClO_4)_2{\cdot}6H_2O$ (26 mg, 0.07 mmol) acetonitrile (1 mL) solution was added during stirring. During the addition, the color of the solution turned from light yellow to blue. After stirring for 1 hour at room temperature, small amount of blue precipitate finally appeared. The reaction was kept stirring for 1 h at room temperature. Slow diffusion of diethyl ether into the resulting blue solution at 8 °C in a fridge gave rise to the blue crystals that are suitable for single crystal X-ray diffraction (Figure S2). Yield: 25 mg, 70%. ESI-MS (CH_3CN, m/z): 197.05400, $[Cu^{II}\text{-tmpa-NH}]^{2+}$. XPS (eV): 935.3, 942.8, 945, 955.1, 963.5. UV-Vis: 257 nm (1.2×10^4 $M^{-1}{\cdot}cm^{-1}$), 692 nm (100 $M^{-1}{\cdot}cm^{-1}$).

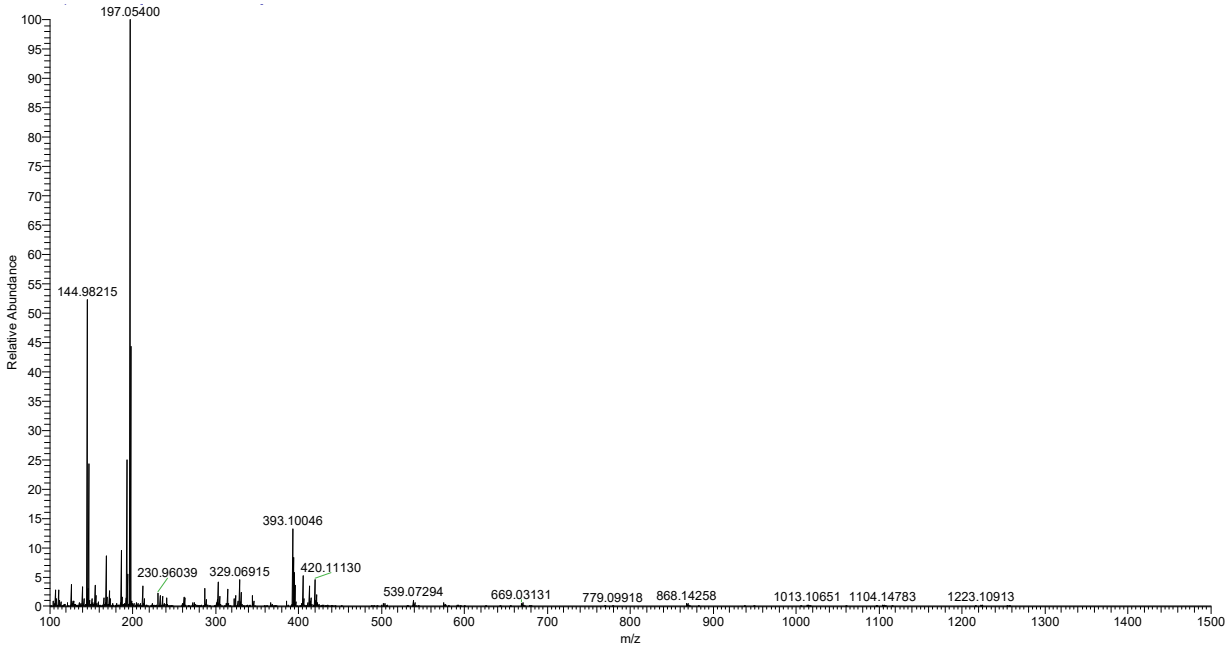

Figure S1. ESI-MS of **$[Cu^{tmpa\text{-}NH}](ClO_4)_2$** in acetonitrile.

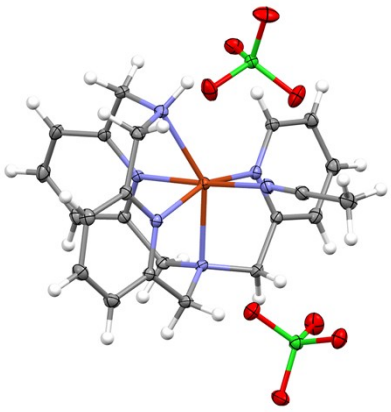

Figure S2. Molecular structure of **$[Cu^{tmpa\text{-}NH}](ClO_4)_2$** determined by X-ray crystallography with thermal ellipsoids drawn at the 30% probability level.

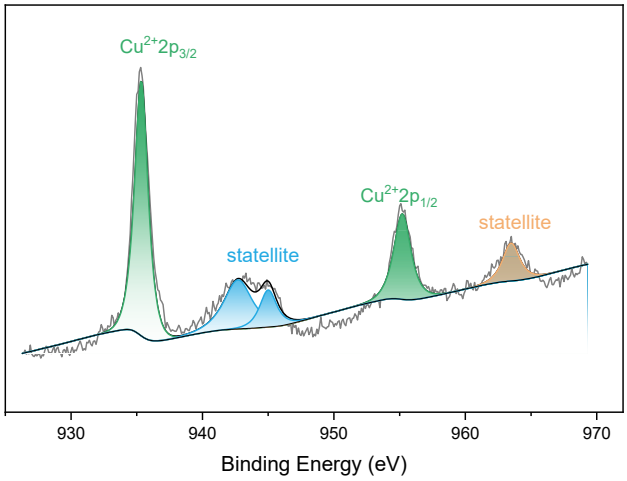

Figure S3. XPS of Cu 2p of **$[Cu^{tmpa\text{-}NH}](ClO_4)_2$**.

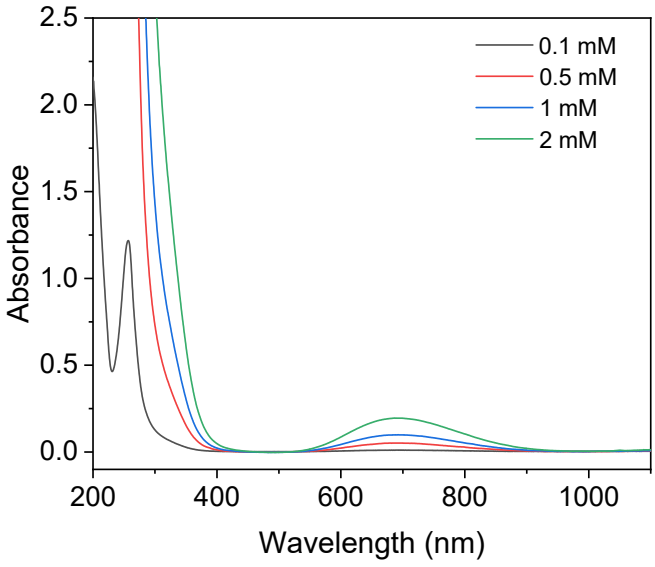

Figure S4. UV-Vis spectra of **$[Cu^{tmpa\text{-}NH}](ClO_4)_2$** in acetonitrile at various concentrations at room temperature. Optical path length: 1 cm.

1.2.2 synthesis of $[Cu^{bmpa\text{-}NH}](ClO_4)_2$

The tetradentate ligand 2,11-diaza[3,3](2,6)pyridinophane (20 mg, 0.083 mmol) was dissolved in acetonitrile (2 mL) in a vial, an acetonitrile (1 mL) solution of $Cu(ClO_4)_2{\cdot}6H_2O$ (32 mg, 0.087 mmol) was added during stirring. During the addition, the color of the solution turned from colorless to blue. After stirring for 1 hour at room temperature, the reaction solution was filtered to remove any insoluble species. Slow diffusion of diethyl ether into the resulting blue filtrate at 20 °C gave rise to the blue crystals that are suitable for single crystal X-ray diffraction (Figure S5). The crystalline material was rinsed with diethyl ether three times and dried under vacuum. Yield: 35 mg, 74%. XPS (eV): 934.8, 942.1, 944.2, 954.7, 962.9. UV-Vis: 257 nm (5858 $M^{-1}{\cdot}cm^{-1}$), 717 nm (43 $M^{-1}{\cdot}cm^{-1}$).

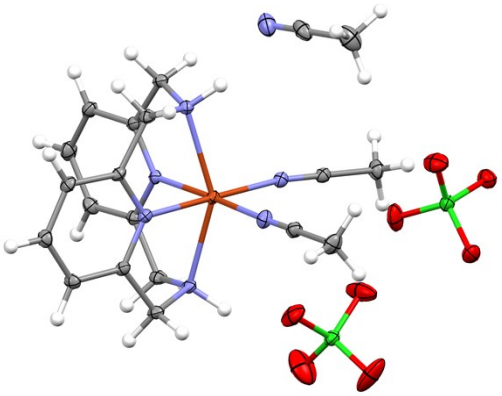

Figure S5. Molecular structure of **[Cu$^{bmpa-NH}$](ClO$_4$)$_2$** determined by X-ray crystallography with thermal ellipsoids drawn at the 30% probability level.

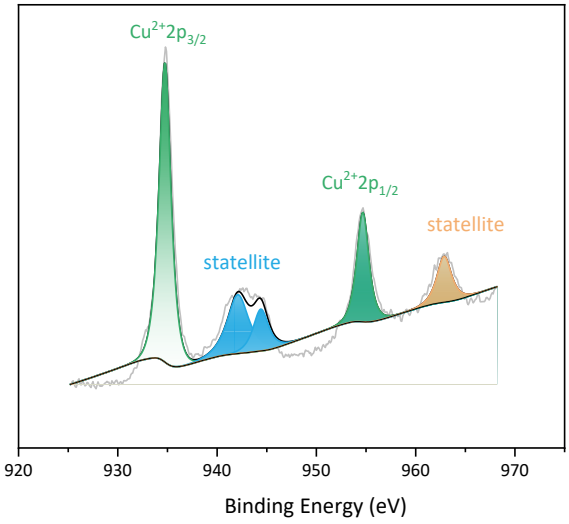

Figure S6. XPS of Cu 2p of **[Cu$^{bmpa-NH}$](ClO$_4$)$_2$**.

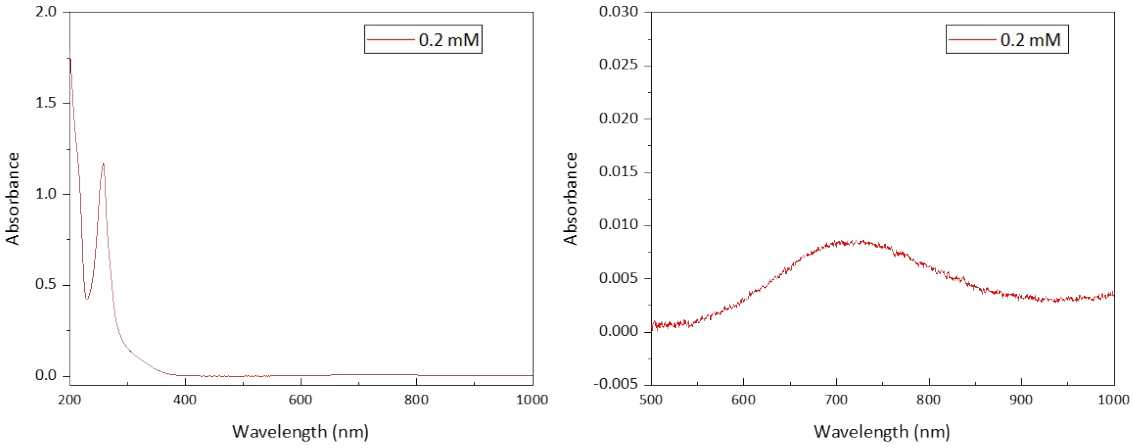

Figure S7. UV-Vis spectra of **[Cu$^{bmpa-NH}$](ClO$_4$)$_2$** in acetonitrile at room temperature.

1.2.3 synthesis of [Cu$^{tmpa\text{-}NH}$]PF$_6$

The pentadentate ligand N-(2-methylpyridine)-2,11-diaza[3.3](2,6)pyridinophane (20 mg, 0.06 mmol) was dissolved in acetonitrile (2 mL) in a vial, an acetonitrile (1 mL) solution of [Cu(MeCN)$_4$]PF$_6$ (25 mg, 0.067 mmol) was added during stirring. During the addition, the color of the solution turned from light yellow to reddish orange. After stirring for 0.5 hour at room temperature, the reaction mixture was filtered to remove insoluble species. Slow diffusion of diethyl ether into the resulting solution at room temperature gave the reddish orange crystals that are suitable for single crystal X-ray diffraction (Figure S12). The crystalline material was rinsed with diethyl ether three times and dried under vacuum. Yield: 22 mg, 68%. ESI-MS (CH_3CN, m/z): 394.10852, [Cu^{I}-tmpa-NH]$^+$. UV-Vis: 250 nm (8752 $M^{-1}\cdot cm^{-1}$), 374 nm (1494 $M^{-1}\cdot cm^{-1}$).

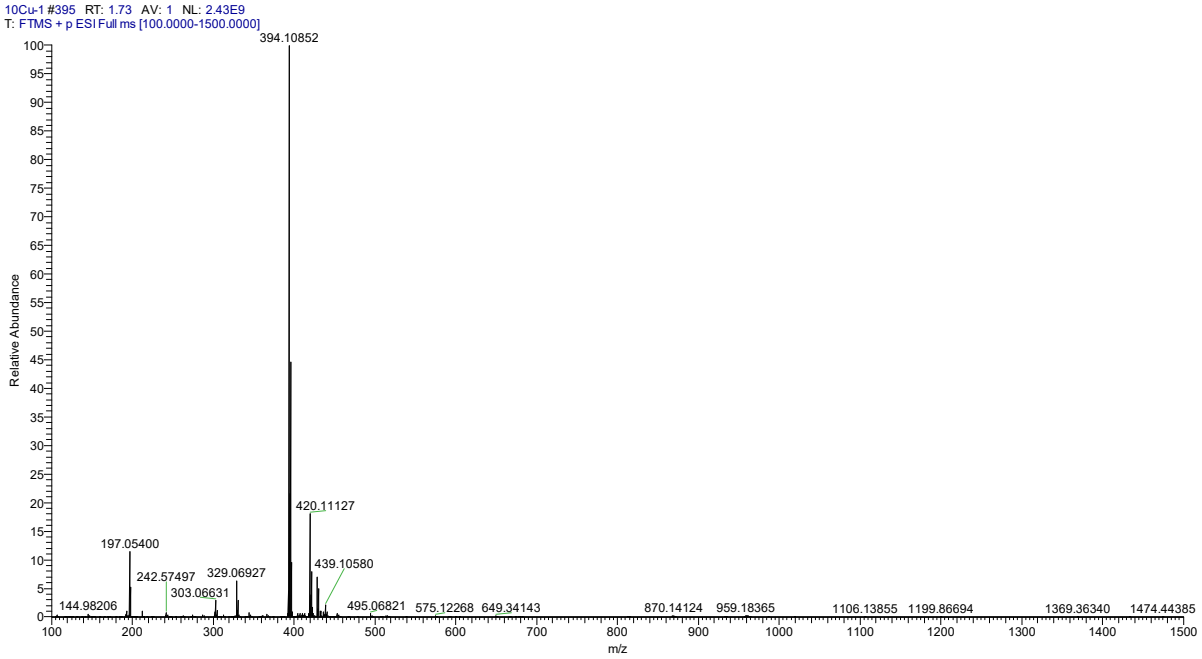

Figure S8. ESI-MS of ***[Cu$^{tmpa\text{-}NH}$]PF$_6$*** in acetonitrile.

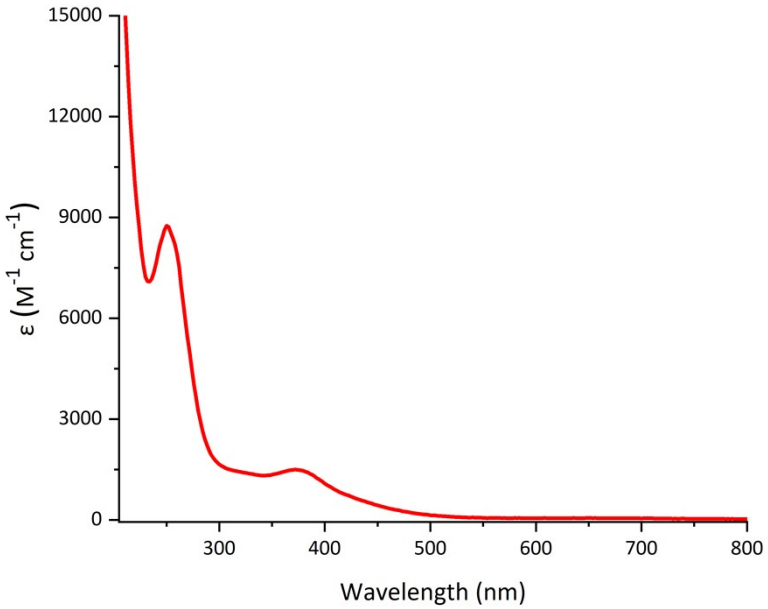

Figure S9. UV-Vis spectra of ***[Cu$^{tmpa\text{-}NH}$]PF$_6$*** in acetonitrile at room temperature.

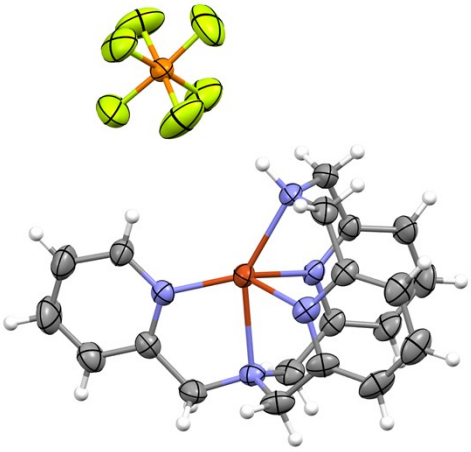

Figure S10. X-ray molecular structure of ***[Cu$^{tmpa-NH}$]PF$_6$*** determined by X-ray crystallography with thermal ellipsoids drawn at the 30% probability level.

1.2.4 synthesis of [Cu$^{bmpa-NH}$]PF$_6$

[Cu$^{bmpa-NH}$]PF$_6$ was prepared according to the literature[6], and characterized by ESI-MS and single crystal X-ray diffraction. ESI-MS (CH_3CN, m/z): 303.06641, [bmpa-NH-Cu(I)]$^+$.

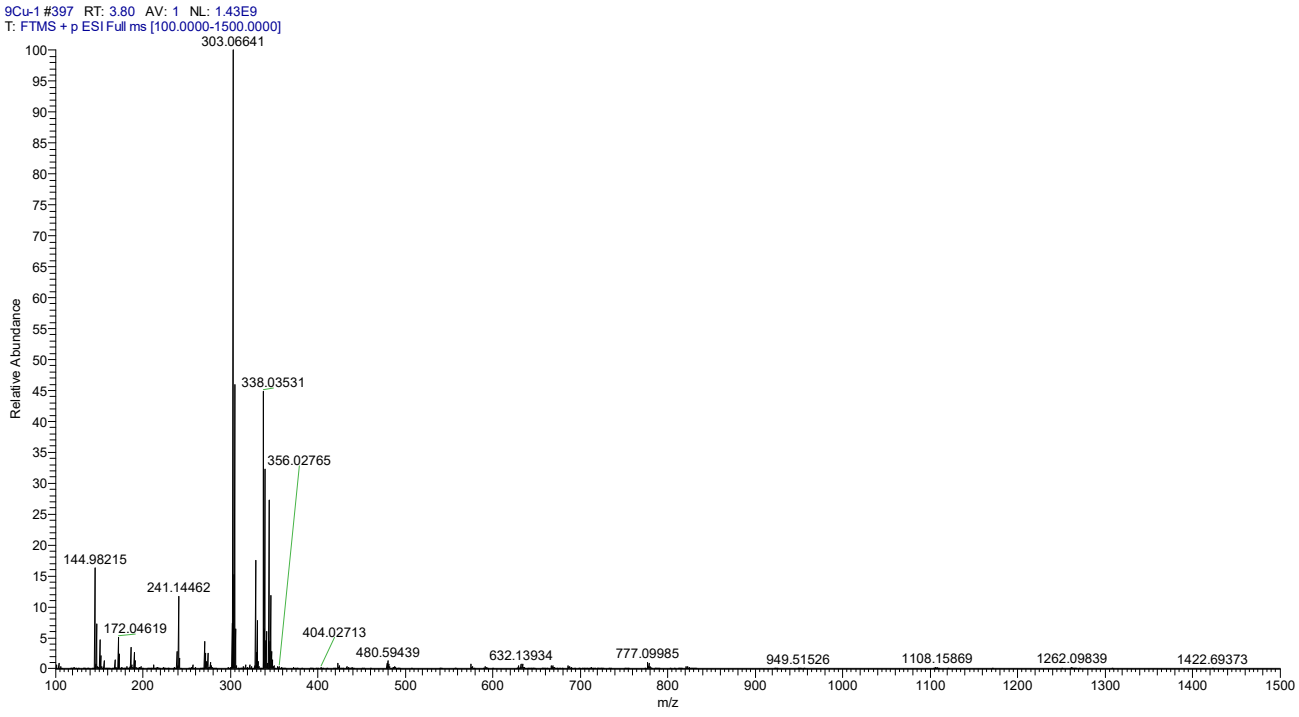

Figure S11. ESI-MS of ***[Cu$^{bmpa-NH}$]PF$_6$*** in acetonitrile.

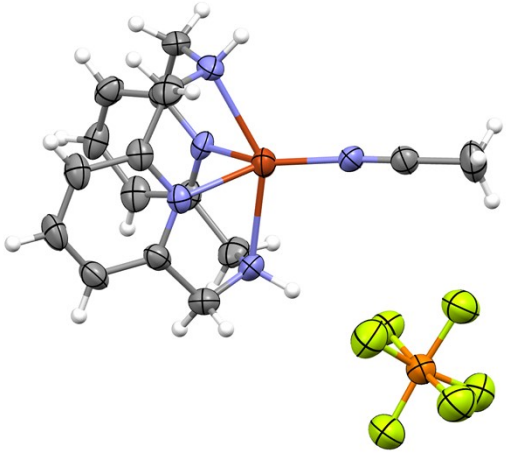

Figure S12. X-ray molecular structure of ***[Cu$^{bmpa\text{-}NH}$]PF$_6$*** determined by X-ray crystallography with thermal ellipsoids drawn at the 30% probability level.

2. Electrochemistry in MeCN

2.1 Cyclic Voltammetry

Cyclic Voltammetry experiments were performed on a CHI Instrument model 760e potentiostat. A standard three-electrode electrochemical cell was used and tetrabutylammonium hexafluorophosphate (n-Bu_4NPF_6) was used as supporting electrolyte. The working electrode was a glassy carbon disk (3 mm in diameter) polished with 2 µm diamond paste for cyclic voltammetry ($E_{p,a}$, anodic peak potential; E_{pc}, cathodic peak potential; $E_{1/2} = (E_{pa} + E_{pc})/2$; $\Delta E_p = E_{pa} - E_{pc}$). The counter electrode was a Pt wire in CH_3CN + 0.1 M Bu_4NPF_6. Potentials were referred to an Ag/0.01 M $AgNO_3$ reference electrode in CH_3CN + 0.1 M Bu_4NPF_6 and measured potentials were calibrated through the use of an internal Fc^+/Fc standard.

2.2 Scan rate dependence

Molecular catalyst was analysed under N_2 atmosphere at various scan rate. Plots of peak potentials as a function of the square root of scan rate were found to be linear correlation, which reveals the freely diffusing characteristic of copper complex in solution and that adsorption on the electrode is negligible under noncatalytic condition according to Randles-Sevcik analysis.

$$i_p = 0.4463 n_p F A [cat] \sqrt{\frac{n_p F \nu D_{cat}}{RT}} \qquad eq.\,S1$$

Where, n_p is the number of electrons transferred to the catalyst from electrode, here taken as 1 (vide infra), i_p is peak current (A) in the absence of substrate, F is Faraday constant (96485.33289 C/mol), A is the active surface area of the electrode (A = 0.0707 cm^2), D_{cat} is the diffusion coefficient of molecular catalyst (cm^2/s), $[cat]$ is the concentration of the catalyst (mol/cm^3), $[cat]$ = 1.0 ×10^{-6} mol/cm^3, ν is the scan rate (V/s), R is the gas constant ($8.3145\ J \cdot K^{-1} \cdot mol^{-1}$), T is the temperature in K (298 K).

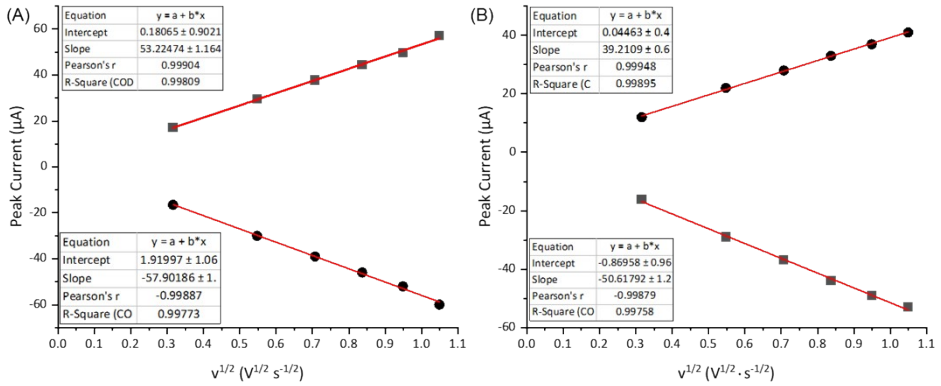

Figure S13 Plots and linear fittings of the oxidative and reductive peak currents of the redox wave in the cyclic voltammograms of (A) **[Cu$^{tmpa-NH}$]**$(ClO_4)_2$ and (B) **Cu$^{bmpa-NH}$]**$(ClO_4)_2$ as a function of square root of scan rate. This behavior is indicative of a freely-diffusing species.

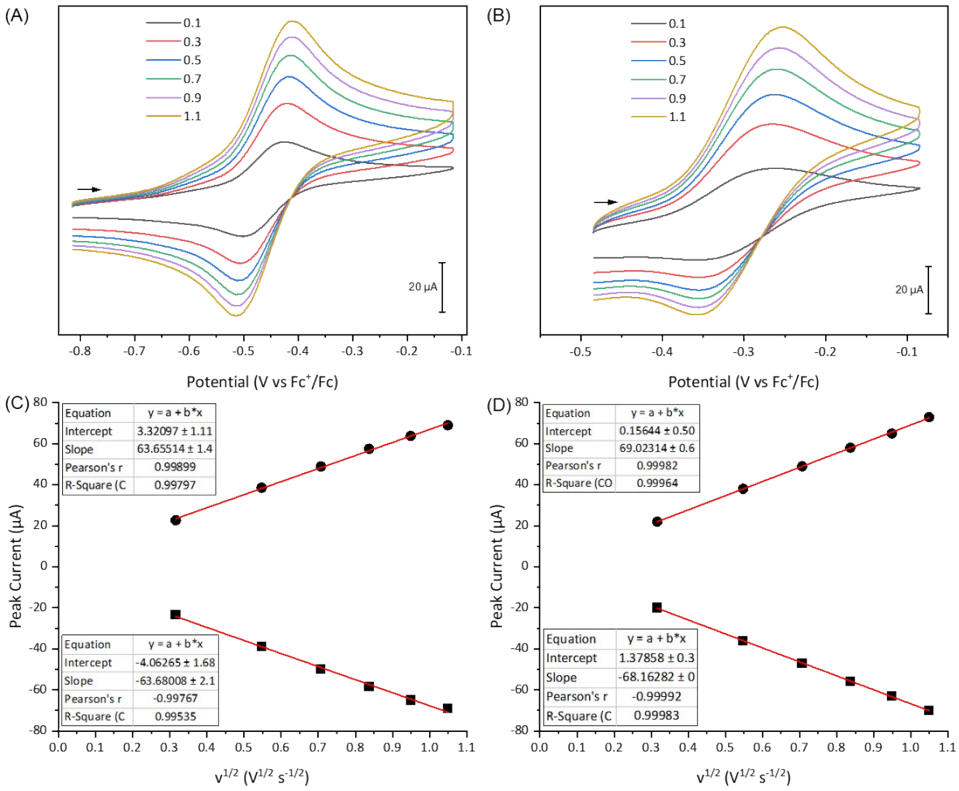

Figure S14 CVs of (A) **[Cu$^{tmpa-NH}$]**PF_6 (1 mM, $E_{1/2}$ = -0.46 V vs Fc^+/Fc with ΔE_p of 78 mV at scan rate of 0.1 V s^{-1}) and (B) **[Cu$^{bmpa-NH}$]**PF_6 (1 mM, $E_{1/2}$ =-0.31 V vs Fc^+/Fc with ΔE_p of 89 mV at scan rate of 0.1 V s^{-1}) in CH_3CN with 0.1 M *n*-Bu_4PF_6 as supporting electrolyte at various scan rates under N_2 atmosphere. Plots and linear fittings of the oxidative and reductive peak currents of the redox wave in the cyclic voltammograms of (C) **[Cu$^{tmpa-NH}$]PF_6** and (D) **[Cu$^{bmpa-NH}$]PF_6** as a function of square root of scan rate. This behavior is indicative of a freely-diffusing species.

2.3 kinetics measurements and calculations

Foot-of-wave analysis (FOWA). The k_{obs} (or turnover frequency, TOF) could be calculated from the catalytic current enhancement method. While the catalytic process should be under pure kinetic condition, and the catalytic plateau current of an S-shaped voltammogram is required. However, this method is limited in ORR

due to the low solubility of O_2 in CH_3CN. In this case, the rate constant is generally underestimated in this method, although the catalytic peak currents are approximated as the plateau current in this work. Foot-of-wave analysis, developed by Savéant, enable the kinetic information to be obtained on catalysts for which a S-shaped catalytic curve with plateau current cannot be obtained.[7] At the onset of the catalytic wave, the catalytic reaction is assumed to be under kinetic conditions. As such, FOWA is not affected by side phenomena, such as substrate consumption, catalyst deactivation. It is therefore especially useful for the ORR, in which substrate consumption plays an important role.

Savéant group demonstrated that the relationship between catalytic current (i_c) and applied potential can be described as eq. S2.[7] The peak current of catalyst in the absence of substrate (i_p) is described in Randles-Sevčik Equation (eq. S1). It is thus convenient to normalize the slope to i_p (eq. S3) to calibrate the catalyst concentration, electrode surface area and diffusion coefficient. A plot of i_c/i_p as a function of $1+\exp\left[F(E-E_{P/Q})/RT\right]$ will yield a straight line for ideal S-shaped catalytic response, the slope of which, give access to k_{obs}.

$$i_c = \frac{n_{cat}[cat]FA\sqrt{D_{cat}k_{obs}}}{1+\exp\left[\frac{F}{RT}*\left(E-E_{P/Q}\right)\right]} \qquad eq.\,S2$$

$$\frac{i_c}{i_p} = \frac{2.24n_{cat}\sqrt{\frac{RT}{Fvn_p}k_{obs}}}{1+\exp\left[\frac{F}{RT}*\left(E-E_{P/Q)}\right)\right]} \qquad eq.\,S3$$

Where i_c is the catalytic current (A) in the presence of substrate, i_p is peak current (A) in the absence of substrate, n_{cat} is the number of electrons transfer in the catalytic reaction, n_p is the number of electrons transferred to the catalyst from electrode, F is Faraday constant (96485.33289 C/mol), k_{obs} is the observed catalytic rate (s^{-1}), $E_{P/Q}$ is the equilibrium potential of the catalyst redox couple, v is the scan rate (V/s), R is the gas constant ($8.3145\,J\cdot K^{-1}\cdot mol^{-1}$), T is the temperature in K.

The initial elemental steps involved in the reaction in this work can be described as shown below,

(1). $Cu(II)+e^-\rightarrow Cu(I)$ $\qquad E{:}E_{Cu(II/I)}$

(2). $Cu(I)+O_2\rightarrow Cu(II)-O_2^{\cdot-}$ $\qquad C{:}k_{O_2}$

(3). $Cu(II)-O_2^{\cdot-}+3e^-+4H^+\rightarrow Cu(II)+2H_2O$ $\qquad E,C$

As the oxygen-involved intermediates such as superoxo, peroxo, hydroperoxo etc are highly unstable and kinetically invisible, we can consider the rate determined step (RDS) involving equilibrium dioxygen binding followed by rate limiting proton transfer. Therefore, the current system can be simplified to an EC' mechanism. The current-potential relationship as derived by Savéant et al for an EC' type catalytic mechanism can be used for the electrochemical kinetics calculation and eq. 3 can be described as eq. S4 once the electron stoichiometry is accounted.[8-9] Here it is important to mention that FOWA considers that the electron transfer kinetics of the process coupled to the catalytic reaction is infinitely fast and thus assumes reversible Nernstian behavior.[10] Nernstian behavior in current complex has been suggested by the scan rate dependence experiments above. The analysis can provide the kinetic information about the rate-limiting step of the chemical steps (C').

$$\frac{i_c}{i_p} = \frac{2.24(n_{cat})^{\sigma}\sqrt{\frac{RT}{Fvn_p}k_{obs}}}{1+\exp\left[\frac{F}{RT}*\left(E-E_{Cu(II/I)}\right)\right]} \qquad eq.S4$$

Where i_c is the catalytic current (A) in the presence of substrate, i_p is peak current (A) in the absence of substrate, n_{cat} is the number of electrons transfer in the catalytic reaction (here taken as 4), n_p is the number of electrons transferred to the catalyst from electrode (here taken as 1), σ is a stoichiometric factor depending on the mechanism ($0.5 \leq \sigma \leq 1$, here taken as 1), F is Faraday constant (96485.33289 C/mol), k_{obs} is the observed catalytic rate (s^{-1}), $E_{Cu(II/I)}$ is the equilibrium potential of the catalyst redox couple, ν is the scan rate (V/s), R is the gas constant ($8.3145\ J\cdot K^{-1}\cdot mol^{-1}$), T is the temperature in K (298 K).

The foot-of-the-wave analysis was done by plotting the ratio of catalytic to non-catalytic current (i_c/i_p) as a function of the mole fraction of reduced catalyst $\{1+\exp\left[F\left(E-E_{Cu(II/I)}\right)/RT\right]\}$. The slope S of this line is related to the k_{obs} or TOF as shown in equation 5. As a result, the k_{obs} or TOF can be obtained via eq. S6.

$$S = 2.24(n_{cat})^{\sigma}\sqrt{\frac{RT}{Fvn_p}k_{obs}} \qquad eq.S5$$

$$k_{obs} = \frac{S^2 Fvn_p}{\left[2.24(n_{cat})^{\sigma}\right]^2 RT} \qquad eq.S6$$

As the low concentration of catalysts and high concentration of substrate in homogenous solution, substrate reacts with the one-electron reduced species once it formed within the reaction diffusion layer. Therefore, all electron transfer steps are considered to occur at the electrode ($\sigma = 1$) and no homogeneous electron transfer takes place between species ($\sigma = 0.5$ for solution electron transfer).[9, 11-12] Given that the TOF will be larger if solution electron transfer is a dominant mechanism for electron transfer(s), these are lower limits in the TOF.

The rate of dioxygen consumption within the reaction diffusion layer can be generally described as follow,

$$rate = -\frac{d[O_2]}{dt} = k_{cat}\cdot[O_2]^{n_{O_2}}\cdot[LutH^+]^{n_{LutH^+}}\cdot[Cu]^{n_{Cu}} = k_{obs}\cdot[Cu]^{n_{Cu}}$$

Where $[O_2]$, $[LutH^+]$ and $[Cu]$ are the concentrations of dioxygen, acid and copper complex, respectively, n_{O_2}, n_{LutH^+} and n_{Cu} are the reaction orders of dioxygen, acid and copper complex, respectively, k_{obs} is the observed catalytic rate (s^{-1}), equals to turnover frequency (TOF) for dioxygen reduction.

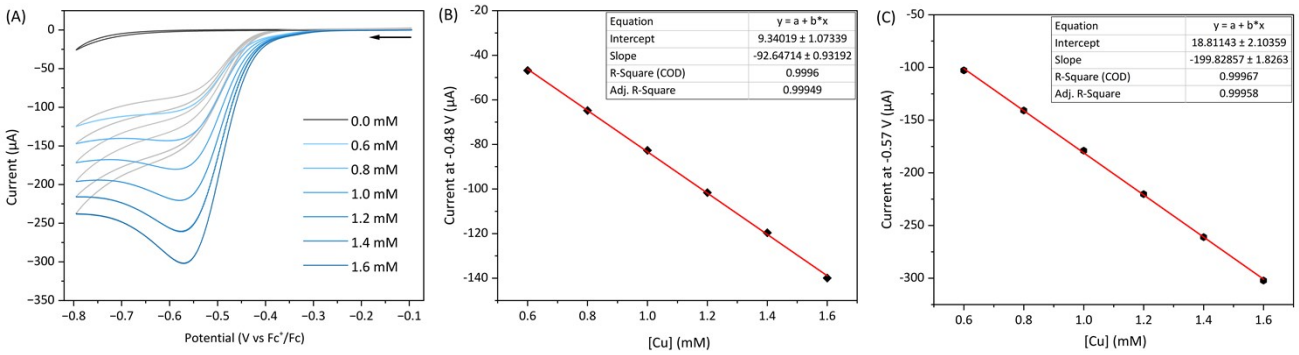

Figure S15 (A) CVs of varied concentrations of **[Cu$^{tmpa-NH}$]**$(ClO_4)_2$ (0, 0.6, 0.8, 1.0, 1.2, 1.4, 1.6 mM) under 1 atm O_2 atmosphere (6 mM) and high concentration of $LutHBF_4$ (160 mM) condition. Scan rate: 100 mV/s. Plots and linear fittings of the catalytic currents at (B) -0.48 V, (C) -0.57 V as a function of the concentrations of **[Cu$^{tmpa-NH}$]**$(ClO_4)_2$. Catalytic currents are directly proportional to [Cu] according to eq. S2.[9]

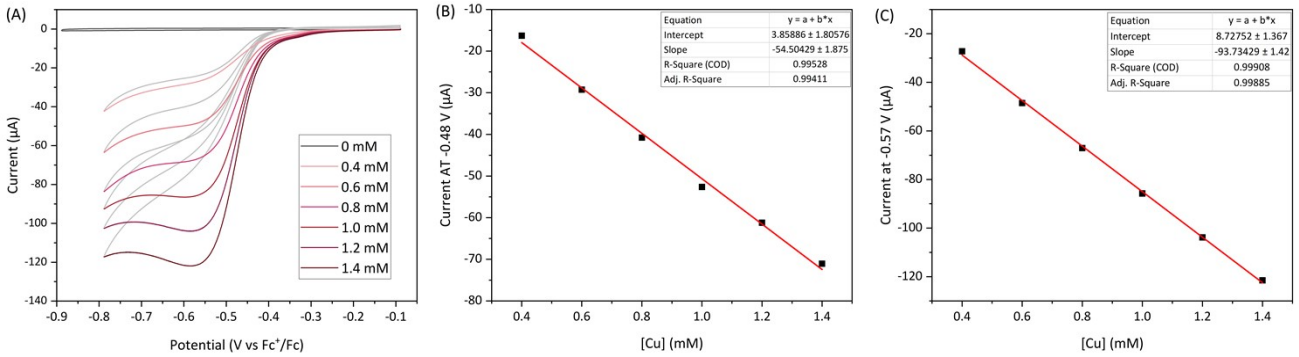

Figure S16 (A) CVs of varied concentrations of **[Cu$^{tmpa-NH}$]**$(ClO_4)_2$ (0, 0.4, 0.6, 0.8, 1.0, 1.2, 1.4 mM) under 1 atm O_2 atmosphere (6 mM) and low concentration of $LutHBF_4$ (20 mM) condition. Scan rate: 100 mV/s. Plots and linear fittings of the catalytic currents at (B) -0.48 V, (C) -0.57 V as a function of the concentrations of **[Cu$^{tmpa-NH}$]**$(ClO_4)_2$. Catalytic currents are directly proportional to [Cu] according to eq. S2.[9]

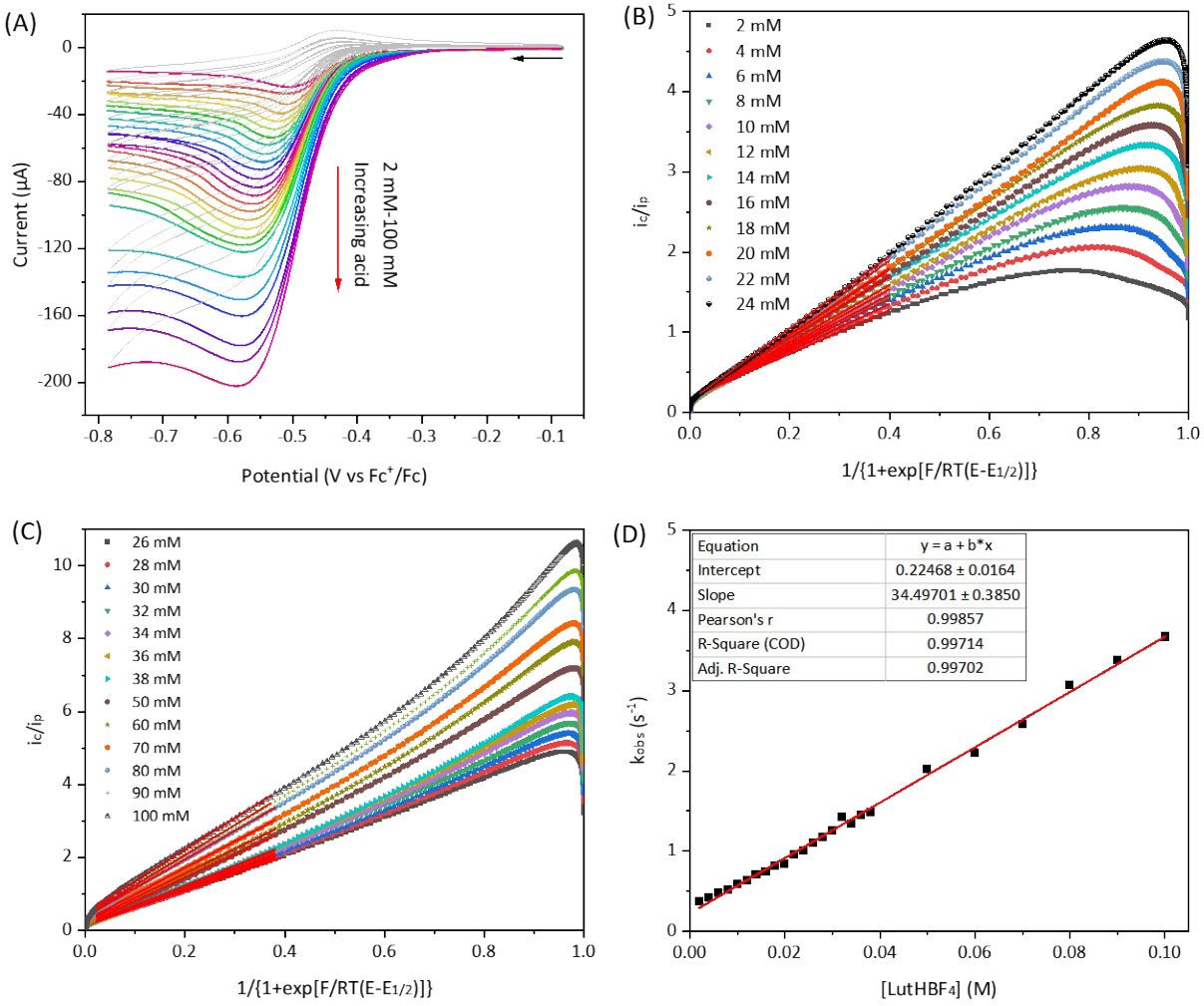

Figure S17 (A) CVs of **[Cu$^{tmpa-NH}$]**$(ClO_4)_2$ (1.0 mM) under 1 atm O_2 atmosphere (6 mM) and varied concentration of $LutHBF_4$ (2~100 mM) condition. Scan rate: 100 mV/s. (B) and (C) Corresponding FOWA plots with red lines indicating fitting regions. The linear fitting regions were fixed in the range of 0.04-0.4 of the $\{1 + \exp[F(E - E_{Cu(II/I)})/RT]\}$. (D)Plots and linear fitting of the k_{obs} derived from FOWA versus [$LutHBF_4$]. The linear correlation reveals the first-order dependence on [$LutHBF_4$] (*i.e.* $n_{LutH^+} = 1$).

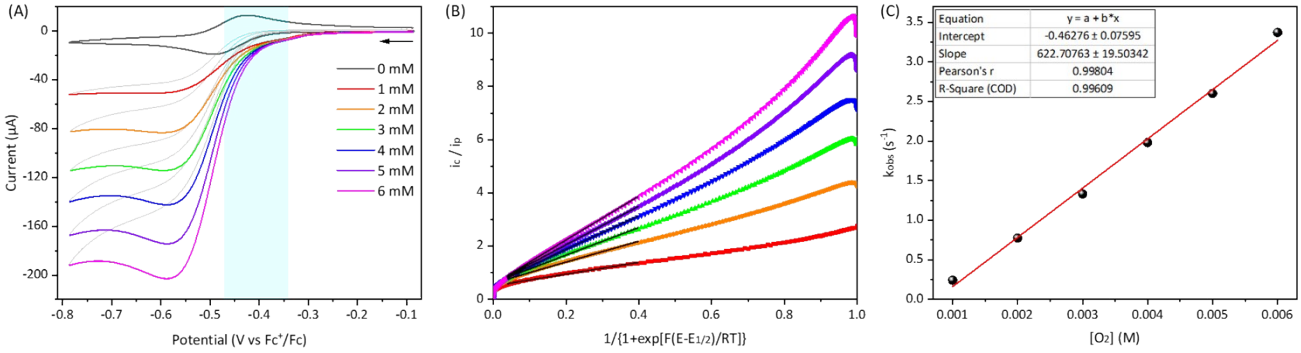

Figure S18 (A) CVs of **[Cu$^{tmpa-NH}$]**$(ClO_4)_2$ (1.0 mM) under high concentration of $LutHBF_4$ (100 mM) and varied concentration of O_2 (0, 1, 2, 4, 5, 6 mM) condition. Scan rate: 100 mV/s. The light blue part represents the potentials window for the linear fitting in the FOWA. (B) Corresponding FOWA plots with black lines indicating fitting regions. The linear fitting regions were fixed in the range of 0.04-0.4 of the $\{1 + \exp[F(E - E_{Cu(II/I)})/RT]\}$. (C) k_{obs} derived from FOWA as a function of [O_2]. The linear correlation reveals the first-order dependence on [O_2] (*i.e.* $n_{O_2} = 1$).

All these results give a rate equation of the form:

$$rate = k_{obs}[Cu] = k_{H^+}[LutHBF_4][Cu] = k_{O_2}[O_2][Cu] = k_{cat}[LutHBF_4][O_2][Cu]$$

where the third-order rate constant k_{cat} is determined to be $(5.75 \pm 0.07) \times 10^3 M^{-2} s^{-1}$ from k_{H^+} and $(6.23 \pm 0.20) \times 10^3 M^{-2} s^{-1}$ from k_{O_2}. These two close values display consistency for the estimation of catalytic rate constant of copper complex, which further confirms the third-order kinetics with the weighted average $k_{cat} = (5.99 \pm 0.14) \times 10^3 M^{-2} s^{-1}$. Therefore, the TOF was calculated to be $3.6 \pm 0.08\ s^{-1}$ in the presence of 100 mM $LutHBF_4$ and 1 atm O_2 (6 mM in acetonitrile containing 0.1 M electrolyte).

i_{cat}/i_p method. To compare the electrocatalytic performance of **[Cu$^{tmpa\text{-}NH}$]**$^{2+}$ with that of **[Cu^{tmpa}]**$^{2+}$ in CH_3CN, the observed catalytic rate k_{obs} was determined from the catalytic current enhancement by applying eq. S7.

$$\frac{i_c}{i_p} = \frac{n_{cat}}{0.4463 n_p^{3/2}} \sqrt{\frac{RT}{Fv} k_{obs}} \qquad eq.S7$$

Where, n_p is the number of electrons transferred to the catalyst from electrode, here taken as 1, i_p is peak current (A) in the absence of substrate, i_c is the catalytic current (A) in the presence of substrate, n_{cat} is the number of electrons transfer in the catalytic reaction, here taken as 4, F is Faraday constant (96485.33289 C/mol), k_{obs} is the observed catalytic rate (s^{-1}), v is the scan rate (V/s), R is the gas constant ($8.3145\ J \cdot K^{-1} \cdot mol^{-1}$), T is the temperature in K (298 K).

2.4 Rotating ring-disk electrode voltammetry

Rotating ring-disk electrode voltammograms (RRDEV) were performed on a CHI Instrument model 760e potentiostat. The working electrode was a Pine Instrument RRDE assembly with a disk of glassy carbon (GC, Ø = 5mm) and a Pt ring (A = 0.1 cm^2, secondary working electrode). The counter electrode was a Pt wire in CH_3CN + 0.1 M Bu_4NPF_6. Potentials were referred to an Ag/0.01 M $AgNO_3$ reference electrode in CH_3CN + 0.1 M Bu_4NPF_6 and measured potentials were calibrated through the use of an internal Fc^+/Fc standard. Experiments were done in the absence of ferrocene, which was added at the end of the experiment as an internal reference. The rotation rate of platinum ring was fixed at 1500 rpm and the potential was set at 0.8 V vs Fc^+/Fc to oxidize the generated H_2O_2.[12] The disk was scanned from -0.1 to -0.9 V at 5 mV/s. Disk and ring currents in the absence of catalysts were subtracted from the disk and ring currents due to background O_2 reduction at the GC disk. The faradaic efficiency for H_2O_2 production as a function of applied potential at the disk is obtained according with equation (S8). The equation (S9) was used to calculate n.

$$\%H_2O_2 = \frac{\frac{2i_{ring}}{N}}{i_{disk} + \frac{i_{ring}}{N}} \times 100 \qquad eq.S8$$

$$n = \frac{4 \times i_{disk}}{i_{disk} + \frac{i_{ring}}{N}} \qquad eq.S9$$

Where i_{ring} and i_{disk} are the absolute values of ring and disk current at potential E, and N is the collection efficiency of the electrode. The collection efficiency (N) was calculated to be 32 % using the one-electron $[Fe(CN)_6]^{3-/4-}$ redox couple (Figure S28). The collection efficiency N_{H2O2} for the Pt ring was further determined as 0.19±0.02 (Figure S30).

RRDE experiments were carried out in acetonitrile (0.1 M Bu_4NPF_6, 10 mM $LutHBF_4$) solution under O_2-saturated atmosphere in the absence and presence of Cu catalyst (0.1 mM).

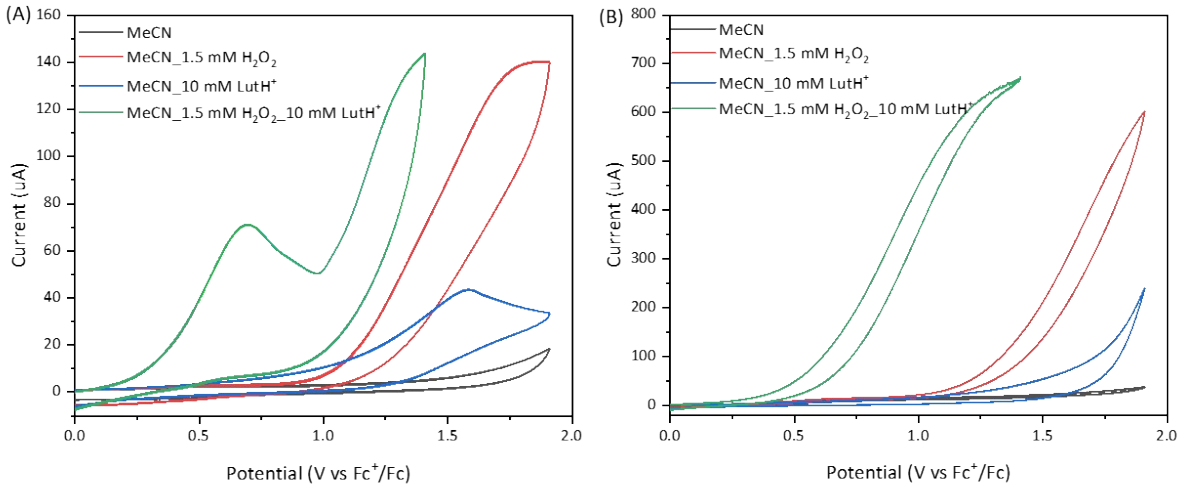

Figure S19. (A) CV measured at the Pt ring electrode in the presence of 1.5 mM H_2O_2 and 10 mM $LutHBF_4$ in MeCN solution. (B) CV measured at the Pt ring electrode in the presence of 1.5 mM H_2O_2 and 10 mM $LutHBF_4$ at a rotation rate of 1500 rpm in MeCN solution. Scan rate 100 mV/s.

It was found that the potential of 0.7-1.4 V vs Fc^+/Fc for Pt ring will be efficient for the oxidation of H_2O_2 in the presence of $LutHBF_4$ under our experimental conditions.

2.5 Controlled-potential electrolysis and iodometric titration

Bulk electrolysis and coulometry experiments were carried out in acetonitrile (5 mL, 0.1 M Bu_4NPF_6, 100 mM ^{LutHBF_4}) solution under O_2-saturated atmosphere in the absence and presence of **[Cu$^{tmpa\text{-}NH}$]**$(ClO_4)_2$ catalyst (1 mM). A graphite rod was used as working electrode (active surface area:1.79 cm^2). According to the electrochemical response, electrolysis was conducted at -0.60 V and -0.69 V for 30 minutes. And the consumed charges were 4.81C (-0.6 V) and 4.36 C (-0.69 V) in the presence of catalyst, which is much higher than those (0.44 C and 0.79 C) of the blank in the absence of catalyst. In the calculation of Faradic efficiency for H_2O_2, the consumed charges have been corrected by subtracting the blank consumed charges.

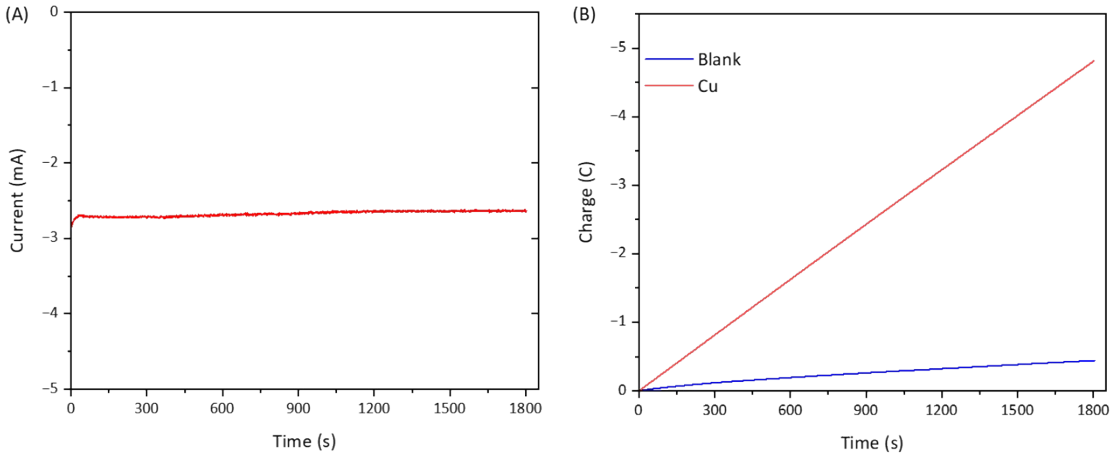

Figure S20. (A) Plots of the current vs the time during the bulk electrolysis at an applied potential of -0.6 V on the O_2-saturated CH_3CN solution (0.1 M Bu_4NPF_6, 100 mM ^{LutHBF_4}) in the presence (red) of **[Cu$^{tmpa\text{-}NH}$]**$(ClO_4)_2$

(1 mM). (B) Plots of the consumed charge vs the time in the absence (blue) and presence (red) of **[Cu$^{tmpa-NH}$]**$(ClO_4)_2$ (1 mM).

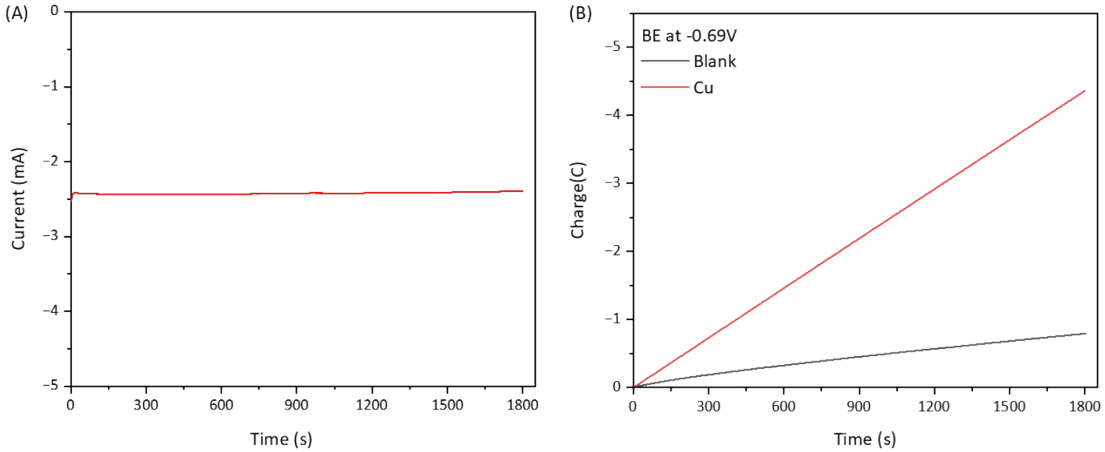

Figure S21. (A) Plots of the current vs the time during the bulk electrolysis at an applied potential of -0.69 V on the O_2-saturated CH_3CN solution (0.1 M Bu_4NPF_6, 100 mM $LutHBF_4$) in the presence (red) of **[Cu$^{tmpa-NH}$]**$(ClO_4)_2$ (1 mM). (B) Plots of the consumed charge vs the time in the absence (black) and presence (red) of **[Cu$^{tmpa-NH}$]**$(ClO_4)_2$ (1 mM).

The quantity of H_2O_2 production after bulk electrolysis was followed to be detected by iodometric titration and analysed via UV-Vis spectroscopy.[13] H_2O_2 can react with the iodine ion (I^-) to generate a triiodide ion (I_3^-) with strong absorbance at 360 nm according to the following chemical equation:

$$iodometric\ titration: 3I^- + H_2O_2 + 2H^+ \rightarrow I_3^- + 2H_2O$$

$$c(H_2O_2) = c(I_3^-)$$

Therefore, the H_2O_2 concentration can be obtained by measuring the I_3^- concentration that can be analysed via UV-Vis spectroscopy. Generally, 1 mL of 0.4 M KI aqueous solution and 1 mL CH_3CN solution containing 100 mM $LutHBF_4$ with varied concentrations of H_2O_2 were mixed and the resulting solution was kept for 30 minutes. Then, UV-Vis spectra were recorded on the above mentioned solutions. The standard curve was established by measuring the absorbance of several solutions of H_2O_2 with known concentrations. A molar absorption coefficient ε of $24137 \pm 298\ M^{-1} \cdot cm^{-1}$ was determined, which is similar with the reported value.[13-16]

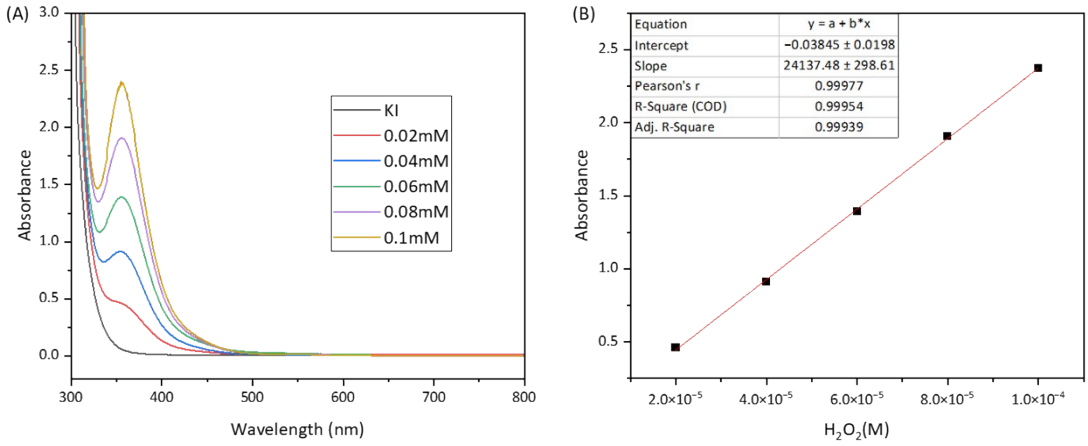

Figure S22. (A) UV-Vis spectra of the mixed solution of 1 mL of 0.4 M KI aqueous solution and 1 mL CH_3CN solution containing 100 mM $LutHBF_4$ with varied concentrations of H_2O_2 (0, 0.02, 0.04, 0.06, 0.08, 0.10 mM), (B) Plots and linear fitting of the absorbance at 360 nm as a function of the concentrations of H_2O_2.

After electrolysis, 1 mL of the electrolyzed CH_3CN solution was mixed with 1 mL of 0.4 M KI aqueous solution and the resulting solution was kept for 30 minutes. Then, UV-Vis spectra were recorded. On the basis of the absorbances and the standard curve, the concentrations of H_2O_2 in the electrolyzed CH_3CN solutions are determined to be 69.67×2 μM (-0.6 V) and 73.56×2 μM (-0.69 V), respectively. The Faradic efficiency of H_2O_2 (H_2O_2%) produced during electrolysis in the presence of copper complex were calculated to be 1.54 % and 1.98 % based on the following equation:

$$FE(H_2O_2) = \frac{n(H_2O_2)}{Q} \times 2F$$

where n is the total amount of H_2O_2 generated during the electrolysis, Q is the charge passed during the electrolysis, and F is the Faraday constant. In the calculation of Faradic efficiency for H_2O_2, Q have been corrected by subtracting the blank consumed charges.

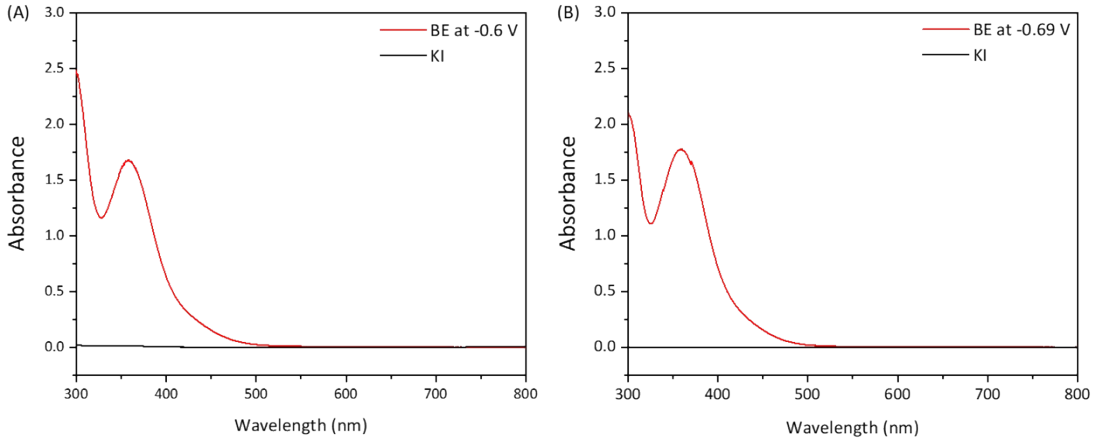

Figure S23. UV-Vis spectra of the mixed solution of 1 mL of 0.4 M KI aqueous solution and 1 mL electrolyzed CH_3CN solution after electrolysis at an applied potential of (A) -0.6 V and (B) -0.69 V on the O_2-saturated CH_3CN solution (0.1 M Bu_4NPF_6, 100 mM $LutHBF_4$) in the presence of **[Cu$^{tmpa\text{-}NH}$]**$(ClO_4)_2$.

Table S1. Catalytic selectivity of oxygen reduction mediated by **[Cu$^{tmpa\text{-}NH}$]**$(ClO_4)_2$ (1.0 mM) via bulk electrolysis in 30 mins.

Applied potential (V vs Fc^+/Fc)	Consumed charge (C)	Generated H_2O_2 (μM)	Faradic efficiency of H_2O_2 (%H_2O_2)
-0.6	4.81	140	1.54
-0.69	4.36	147	1.98

2.6 Rinse test

Contributions from adsorption were tested for **[Cu$^{tmpa-NH}$]**$(ClO_4)_2$ by use of a rinse test. After catalytic runs, the electrode was taken out of solution, rinsed with fresh acetonitrile containing 0.1 M Bu_4NPF_6, and immersed in a fresh acetonitrile containing 0.1 M Bu_4NPF_6. The scans obtained resulted in absolutely no catalytic current within the potential window of interest to evaluate homogeneous catalytic turnover frequencies.

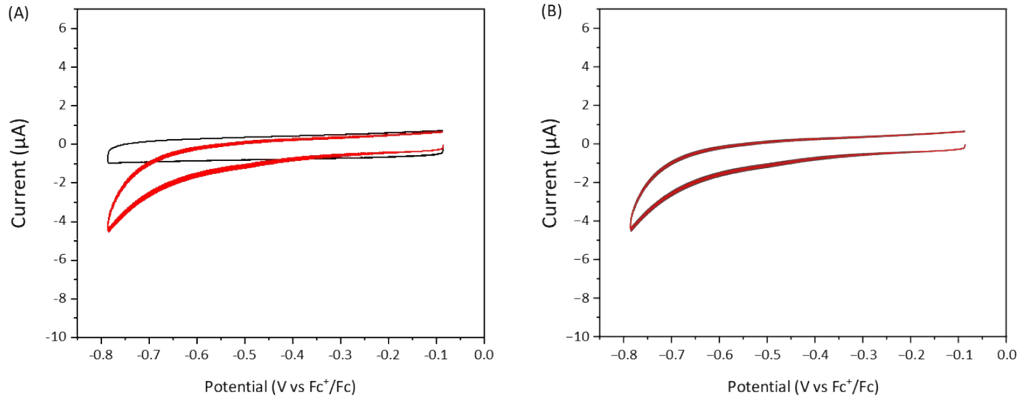

Figure S24. (A) CVs of blank solution under N_2 (blank curve) and O_2 (red curve) atmosphere, (B) rinse test: CVs of the used GC electrode after rinsing in the fresh electrolyte solution. Scan rate: 100 mV/s, electrolyte: 0.1 M Bu_4NPF_6, 3 mm diameter of GC electrode.

2.7 Stability test

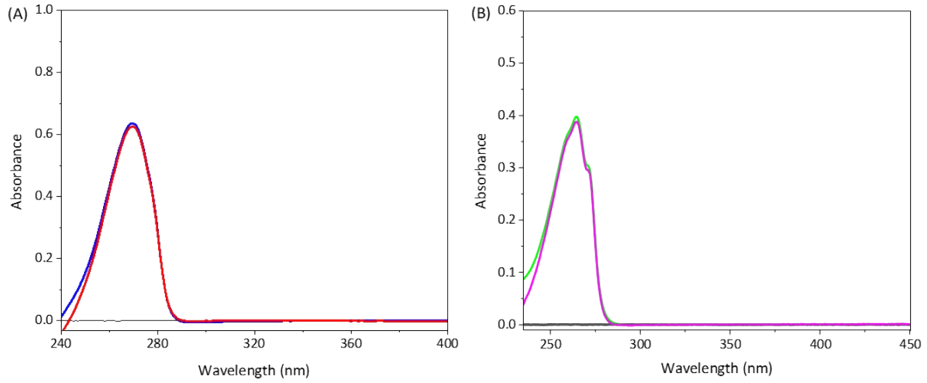

Figure S25. UV-Vis spectra of (A) ^{LutHBF_4} (0.1mM) in the absence (blue) and presence (red) of H_2O_2 (10 mM) and (B) lutidine (0.1mM) in the absence (green) and presence (magenta) of H_2O_2 (10 mM) in MeCN. Path length: 1 cm. The super little change on the absorbance at 270 nm and 265 nm should stem from the volume variation caused by adding the stock solution of H_2O_2. Thus, they are stable in the presence of H_2O_2.

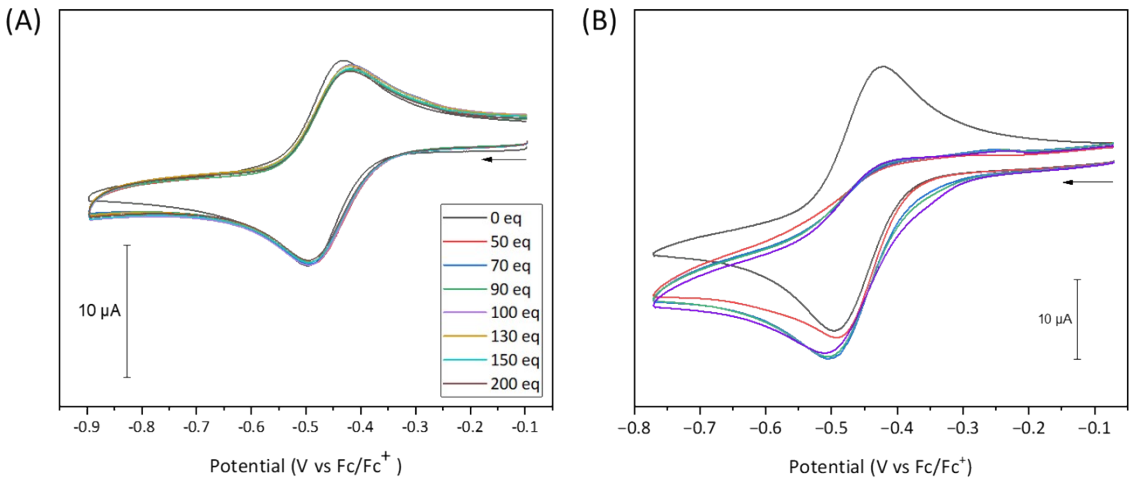

Figure S26. (A) CVs of **[Cu$^{tmpa-NH}$]**$(ClO_4)_2$ (0.5 mM) in the absence (black) and presence of various amount of $LutHBF_4$ in MeCN under N_2 atmosphere. (B) CVs of **[Cu$^{tmpa-NH}$]**$(ClO_4)_2$ (1 mM) in the absence (black) and presence (red) of H_2O_2 (6 mM) in MeCN under N_2 atmosphere. CVs of **[Cu$^{tmpa-NH}$]**$(ClO_4)_2$ (1 mM) in the presence of H_2O_2 (6 mM) after adding various amount of $LutHBF_4$ (blue: 10 mM, green: 20 mM, violet: 100 mM). Scan rate: 100 mV/s, electrolyte: 0.1 M Bu_4NPF_6, 3 mm diameter of GC electrode.

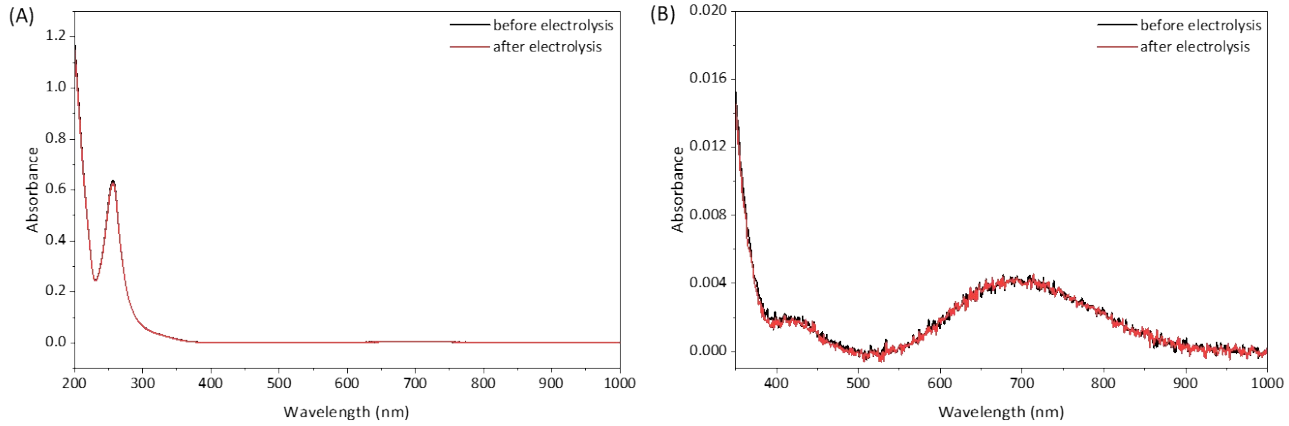

Figure S27. UV-Vis spectra of (A) **[Cu$^{tmpa-NH}$]**$(ClO_4)_2$ (0.05 mM) before and after electrolysis at -0.6 V vs Fc/Fc^+ in MeCN. Path length: 1 cm.

3. electrochemistry in aqueous media

Cyclic Voltammetry experiments were performed on a CHI Instrument model 760e potentiostat. A standard three-electrode electrochemical cell was used. A standard Ag/AgCl electrode in a saturated KCl solution was used as reference electrode. The working electrode was a glassy carbon disk (3 mm in diameter) polished with 2 µm diamond paste for cyclic voltammetry. A Pt wire was used as the counter electrode. A phosphate buffer (PB) solution at pH 7, containing 100 mM phosphate salts (Na_2HPO_4, NaH_2PO_4), was used as supporting electrolyte solution. For RRDEV, the working electrode was a Pine Instrument RRDE assembly with a disk of glassy carbon (GC, Ø = 5mm) and a Pt ring (A = 0.1 cm^2, secondary working electrode). The rotation rates range from 400 RPM to 2800 RPM, 400 RPM increments. Disk and ring currents in the absence of catalysts were subtracted from the disk and ring currents due to background O_2 reduction at the GC disk. The faradaic efficiency for H_2O_2 production as a function of applied potential at the disk is obtained according with equation (S8). The equation (S9) was used to calculate n.

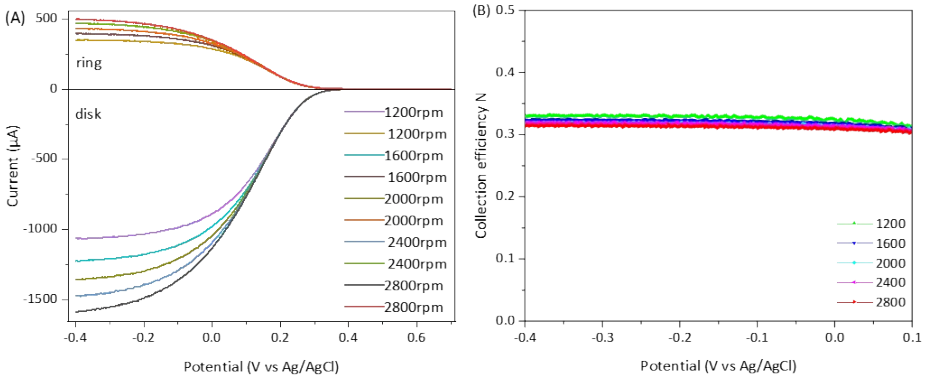

Figure S28. (A) RRDEV of 10 mM $K_3Fe(CN)_6$ in PB (pH = 7) solution at different rotation rates from 1200 RPM to 2800 RPM, 400 RPM increments. (B) The collection efficiency of the Pt ring electrode determined from the data in (A), which gives a collection efficiency of 0.32±0.016. Scan rate 50 mV/s.

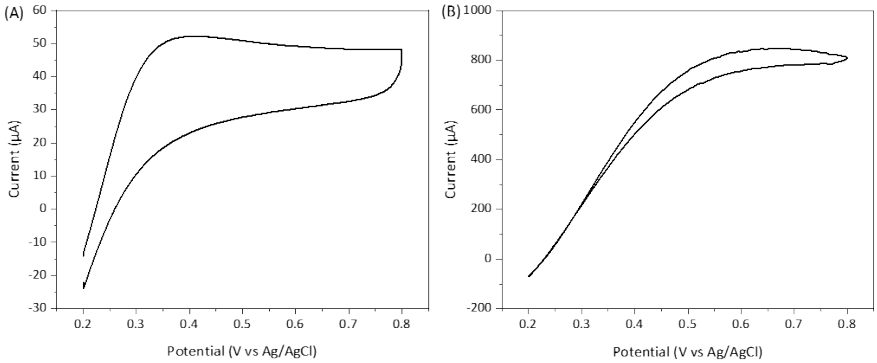

Figure S29. (A) CV measured at the Pt ring electrode in the presence of 1.5 mM H_2O_2 in PB (pH = 7) solution. (B) CV measured at the Pt ring electrode in the presence of 1.5 mM H_2O_2 at a rotation rate of 1600 rpm in PB (pH = 7) solution. Scan rate 100 mV/s.

It was found that 0.5-0.7 V vs Ag/AgCl for Pt ring is an efficient potential for the oxidation of H_2O_2 under our experimental conditions.

Koutecky-Levich analysis

The electron-transfer number of the ORR by GC electrode under our conditions was established by performing a Koutecky-Levich analysis as previously described.[11] The limiting currents at different rotation rates for the ORR show good linearity in accordance with the behaviour described by the Koutecky-Levich equation:

$$\frac{1}{i} = \frac{1}{i_K} + \frac{1}{i_L}$$

Where i_K is the kinetic current and i_L is the mass-transport limited current. i_L can be described through the Levich equation:

$$i_L = 0.62nFAD^{\frac{2}{3}}\nu^{\frac{-1}{6}}C\omega^{\frac{1}{2}} = B \cdot \omega^{\frac{1}{2}}$$

Where n is the electron transfer number, F is the faradaic constant (C/mol), A is the surface area of the disk

electrode (cm^2), D is the diffusion coefficient of O_2 (cm^2/s), ν is the kinematic viscosity (cm^2/s), C is the concentration of O^2 (mol/cm^3), and ω the rotation rate (rad/s). These constants can be simplified with the Levich constant B. The linear relationship observed in the Koutecky-Levich plot provides a B value according to following equation:

$$slope = \frac{1}{B}$$

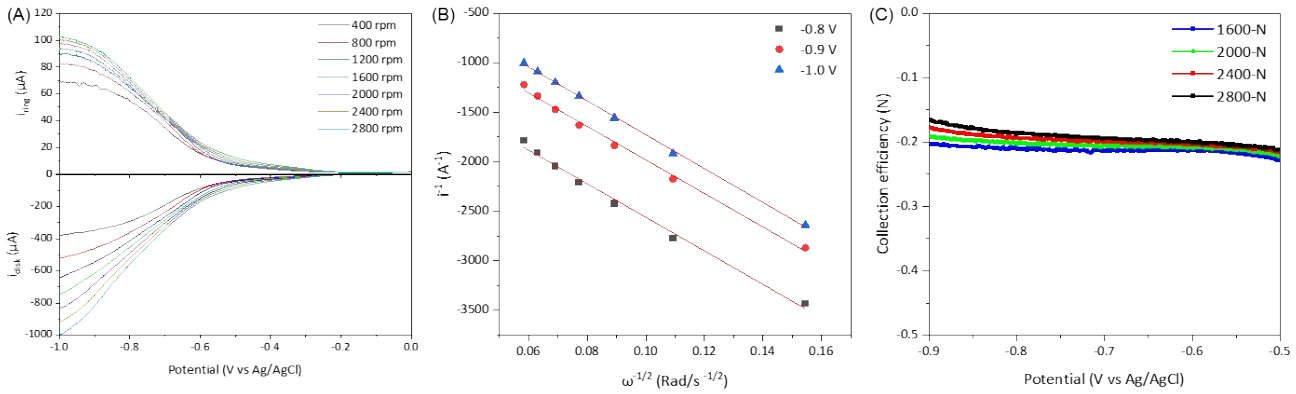

Figure S30. (A) RRDEV of bare electrodes in PB (pH = 7) solution under 1 atm O_2 at different rotation rates from 400 RPM to 2800 RPM, 400 RPM increments. The Pt ring was held at 0.6 V vs Ag/AgCl. Scan rate 50 mV/s. (B) the KL plots of the inverse limiting current (I_L^{-1}) as a function of the inverse square root of the rotation rate. (C) The calculated collection efficiency N_{H2O2} at various rotation rates and potentials for the Pt ring based on the data in (A) and the equation S9.

The KL plots in Figure S32B yield an electron transfer number (n) of 2.36 for the GC disk-catalyzed O_2 reduction. Based on the equation S9 and the currents of disk and ring in Figure S32A, the collection efficiency N_{H2O2} for the Pt ring was determined as 0.19±0.02.

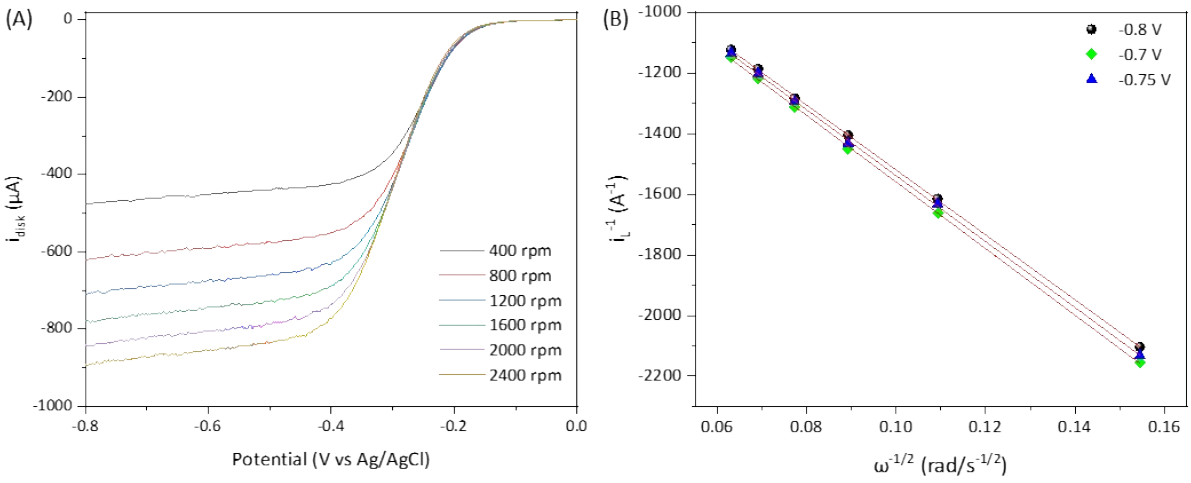

Figure S31. (A) Rotating disk electrode voltammograms (RDEV) of O_2 (1 atm) in the presence of **$[Cu^{tmpa\text{-}NH}]^{2+}$** (0.3 mM) at ambient temperature. Conditions: pH 7 PB solution, scan rate: 50 mV/s. The rotation rates range from 400 RPM to 2400 RPM, 400 RPM increments. (B) the KL plots of the inverse limiting currents (I_L^{-1}) at -0.8, -0.75 and -0.7 V as a function of the inverse square root of the rotation rates.

The KL plots in Figure S33B yield an electron transfer number (n) involved in the homogeneous ORR catalyzed

by **[Cu$^{tmpa-NH}$]**$^{2+}$ was determined to be 3.85±0.05.

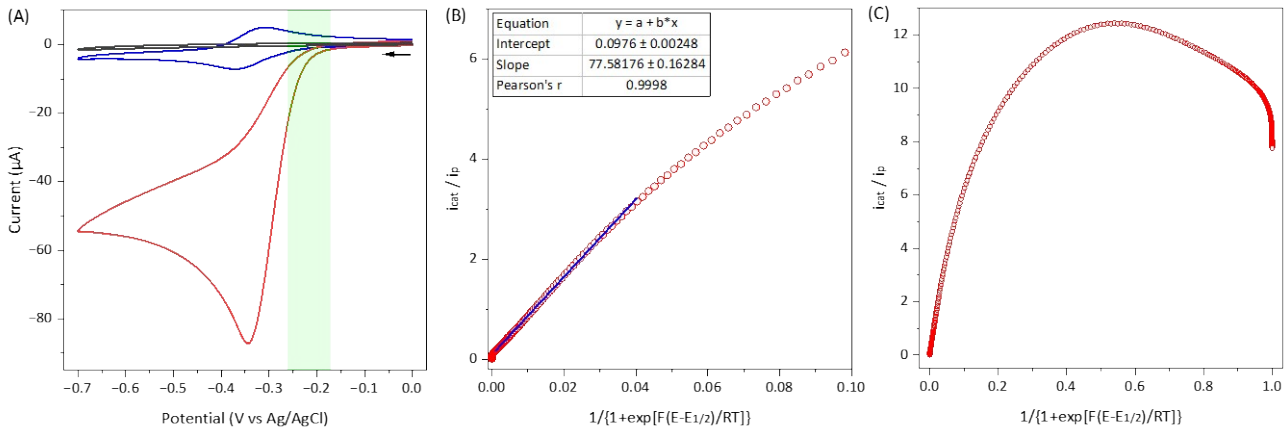

Figure S32. (A) CVs of **[Cu$^{tmpa-NH}$]**$(ClO_4)_2$ (0.32 mM) under N_2 (1 atm, blue) and O_2 (1 atm, red) atmosphere at room temperature. Conditions: pH 7 PB solution, scan rate: 0.1 V/s. Control CV in the absence of catalyst are also shown in black under N_2 atmosphere. The light green part represents the potentials window for the linear fitting in the FOWA. (B) Corresponding FOWA plots with blue line indicating fitting region. (C) Corresponding FOWA plots.

4. Crystallographic data

Table S2. Crystal data and structure refinement of **[Cu$^{tmpa-NH}$]**$(ClO_4)_2$ and **[Cu$^{bmpa-NH}$]**$(ClO_4)_2$.

Identification code	**[Cu$^{tmpa-NH}$]**$(ClO_4)_2$	**[Cu$^{bmpa-NH}$]**$(ClO_4)_2$
Empirical formula	$C_{22}H_{24}Cl_2CuN_6O_8$	$C_{20}H_{25}Cl_2CuN_7O_8$
Formula weight	634.91	625.91
Temperature/K	120.1(3)	120
Crystal system	monoclinic	monoclinic
Space group	$P2_1/n$	$P2_1/n$
a/Å	11.17723(12)	11.5047(4)
b/Å	15.9049(2)	15.2089(6)
c/Å	15.34608(19)	15.8184(6)
α/°	90	90
β/°	95.2960(11)	106.047(3)
γ/°	90	90
Volume/Å^3	2716.47(6)	2659.96(18)
Z	4	4
ρ_{calc}g/cm^3	1.552	1.563
μ/mm^{-1}	3.448	3.520
F(000)	1300.0	1284.0

Crystal size/mm^3	0.36 × 0.28 × 0.18	0.32 × 0.29 × 0.25
Radiation	Cu Kα (λ = 1.54184)	CuKα (λ = 1.54178)
2Θ range for data collection/°	8.024 to 153.474	12.556 to 139.574
Index ranges	-13 ≤ h ≤ 14, -19 ≤ k ≤ 19, -18 ≤ l ≤ 19	-13 ≤ h ≤ 12, -14 ≤ k ≤ 18, -18 ≤ l ≤ 13
Reflections collected	18295	12829
Independent reflections	5515 [R_{int} = 0.0405, R_{sigma} = 0.0274]	4829 [R_{int} = 0.0146, R_{sigma} = 0.0163]
Data/restraints/parameters	5515/0/353	4829/0/346
Goodness-of-fit on F^2	1.049	1.035
Final R indexes [I>=2σ (I)]	R_1 = 0.0434, wR_2 = 0.1187	R_1 = 0.0323, wR_2 = 0.0829
Final R indexes [all data]	R_1 = 0.0444, wR_2 = 0.1195	R_1 = 0.0350, wR_2 = 0.0848
Largest diff. peak/hole / e Å^{-3}	0.59/-0.88	0.51/-0.49

Table S3 Bond Lengths of **[Cu$^{tmpa-NH}$]**$(ClO_4)_2$ and **[Cu$^{bmpa-NH}$]**$(ClO_4)_2$.

[Cu$^{tmpa-NH}$]$(ClO_4)_2$			**[Cu$^{bmpa-NH}$]**$(ClO_4)_2$		
Atom	**Atom**	**Length/Å**	**Atom**	**Atom**	**Length/Å**
Cu1	N1	2.2825(17)	Cu1	N1	2.2968(16)
Cu1	N2	2.0559(17)	Cu1	N2	1.9993(17)
Cu1	N3	2.3083(18)	Cu1	N3	2.3121(16)
Cu1	N4	1.9877(19)	Cu1	N4	2.0305(16)
Cu1	N5	2.0545(19)	Cu1	N5	1.9965(18)
Cu1	N6	1.9973(18)	Cu1	N6	2.0027(18)

Table S4 Bond Angles of **[Cu$^{tmpa-NH}$]**$(ClO_4)_2$ and **[Cu$^{bmpa-NH}$]**$(ClO_4)_2$.

[Cu$^{tmpa-NH}$]$(ClO_4)_2$				**[Cu$^{bmpa-NH}$]**$(ClO_4)_2$			
Atom	**Atom**	**Atom**	**Angle/°**	**Atom**	**Atom**	**Atom**	**Angle/°**
N1	Cu1	N3	150.11(6)	N4	Cu1	N1	78.89(6)
N2	Cu1	N1	78.91(6)	N4	Cu1	N3	78.42(6)
N2	Cu1	N3	77.56(7)	N1	Cu1	N3	149.92(6)
N4	Cu1	N1	80.08(7)	N5	Cu1	N6	89.73(7)
N4	Cu1	N2	85.04(7)	N5	Cu1	N2	179.32(7)
N4	Cu1	N3	79.77(7)	N5	Cu1	N1	100.94(6)
N4	Cu1	N5	92.43(7)	N5	Cu1	N3	100.40(6)
N4	Cu1	N6	159.24(7)	N5	Cu1	N4	94.78(7)
N5	Cu1	N1	105.47(7)	N2	Cu1	N6	90.36(7)

[Cu$^{tmpa-NH}$]$(ClO_4)_2$				**[Cu$^{bmpa-NH}$]**$(ClO_4)_2$			
Atom	**Atom**	**Atom**	**Angle/°**	**Atom**	**Atom**	**Atom**	**Angle/°**
N5	Cu1	N2	174.52(7)	N2	Cu1	N3	78.93(6)
N5	Cu1	N3	97.22(7)	N2	Cu1	N1	79.71(6)
N6	Cu1	N1	79.46(7)	N2	Cu1	N4	85.13(6)
N6	Cu1	N2	94.45(7)	N6	Cu1	N1	100.44(7)
N6	Cu1	N3	120.46(7)	N6	Cu1	N3	100.62(7)
N6	Cu1	N5	89.64(7)	N6	Cu1	N4	175.49(7)

Table S5 Crystal data and structure refinement of **[Cu$^{tmpa-NH}$]**PF_6 and **[Cu$^{bmpa-NH}$]**PF_6.

Identification code	**[Cu$^{tmpa-NH}$]**PF_6	**[Cu$^{bmpa-NH}$]**PF_6
Empirical formula	$C_{20}H_{21}CuF_6N_5P$	$C_{16}H_{19}CuF_6N_5P$
Formula weight	539.93	489.87
Temperature/K	296.15	296.15
Crystal system	monoclinic	orthorhombic
Space group	$P2_1/n$	Pbca
a/Å	7.9276(15)	12.198(12)
b/Å	15.221(3)	15.642(16)
c/Å	18.967(4)	21.79(2)
α/°	90	90
β/°	90.160(3)	90
γ/°	90	90
Volume/Å^3	2288.7(7)	4157(7)
Z	4	8
ρ_{calc}g/cm^3	1.567	1.565
μ/mm^{-1}	1.091	1.192
F(000)	1096.0	1984.0
Crystal size/mm^3	0.35 × 0.12 × 0.11	0.32 × 0.24 × 0.09
Radiation	MoKα (λ = 0.71073)	MoKα (λ = 0.71073)
2Θ range for data collection/°	2.148 to 54.934	3.728 to 49.992
Index ranges	-10 ≤ h ≤ 10, -17 ≤ k ≤ 18, -23 ≤ l ≤ 23	-14 ≤ h ≤ 14, -18 ≤ k ≤ 18, -22 ≤ l ≤ 25
Reflections collected	18539	18177
Independent reflections	4917 [R_{int} = 0.0550, R_{sigma} = 0.0618]	3626 [Rint = 0.1035, Rsigma = 0.0725]
Data/restraints/parameters	4917/0/299	3626/510/318

Goodness-of-fit on F^2	1.015	1.036
Final R indexes [I>=2σ (I)]	R1 = 0.0509, wR2 = 0.1207	R_1 = 0.0626, wR_2 = 0.1494
Final R indexes [all data]	R1 = 0.0888, wR2 = 0.1392	R_1 = 0.1129, wR_2 = 0.1794
Largest diff. peak/hole / e $Å^{-3}$	0.46/-0.38	0.44/-0.42

Table S6 Bond Lengths of **[Cu$^{tmpa-NH}$]**PF_6 and **[Cu$^{bmpa-NH}$]**PF_6..

[Cu$^{tmpa-NH}$]PF_6			**[Cu$^{bmpa-NH}$]**PF_6		
Atom	**Atom**	**Length/Å**	**Atom**	**Atom**	**Length/Å**
Cu1	N1	2.414(4)	Cu1	N1	2.384(5)
Cu1	N2	2.110(3)	Cu1	N2	2.120(4)
Cu1	N3	2.257(4)	Cu1	N3	2.359(5)
Cu1	N4	2.086(4)	Cu1	N4	2.082(4)
Cu1	N5	1.947(4)	Cu1	N5	1.885(5)

Table S7 Bond Angles of **[Cu$^{tmpa-NH}$]**PF_6 and **[Cu$^{bmpa-NH}$]**PF_6.

[Cu$^{tmpa-NH}$]PF_6				**[Cu$^{bmpa-NH}$]**PF_6			
Atom	**Atom**	**Atom**	**Angle/°**	**Atom**	**Atom**	**Atom**	**Angle/°**
N2	Cu1	N1	76.20(13)	N2	Cu1	N1	76.10(18)
N2	Cu1	N3	78.41(14)	N2	Cu1	N3	77.44(17)
N2	Cu1	N4	83.25(14)	N2	Cu1	N4	83.94(17)
N3	Cu1	N1	146.98(14)	N3	Cu1	N1	145.08(16)
N4	Cu1	N1	77.68(15)	N4	Cu1	N1	77.42(19)
N4	Cu1	N3	78.69(16)	N4	Cu1	N3	77.50(18)
N5	Cu1	N1	79.71(15)	N5	Cu1	N2	136.03(19)
N5	Cu1	N2	128.07(16)	N5	Cu1	N1	103.8(2)
N5	Cu1	N3	133.11(15)	N5	Cu1	N3	111.08(19)
N5	Cu1	N4	134.63(16)	N5	Cu1	N4	139.70(19)

Reference:

[1]. Wessel, A. J.; Schultz, J. W.; Tang, F.; Duan, H.; Mirica, L. M., Improved synthesis of symmetrically & asymmetrically N-substituted pyridinophane derivatives. *Org. Biomol. Chem.,* **2017**, *15* (46), 9923-9931.

[2]. Wang, P.; Liang, G.; Boyd, C. L.; Webster, C. E.; Zhao, X., Catalytic H2 Evolution by a Mononuclear Cobalt Complex with a Macrocyclic Pentadentate Ligand. *Eur. J. Inorg. Chem.,* **2019**, *2019* (15), 2134-2139.

[3]. Dolomanov, O. V.; Bourhis, L. J.; Gildea, R. J.; Howard, J. A. K.; Puschmann, H., OLEX2: a complete structure solution, refinement and analysis program. *J. Appl. Crystallogr.,* **2009**, *42* (2), 339-341.

[4]. Sheldrick, G., SHELXT - Integrated space-group and crystal-structure determination. *Acta Crystallogr. Sect. A,* **2015**, *71* (1), 3-8.
[5]. Sheldrick, G., Crystal structure refinement with SHELXL. *Acta Crystallogr. Sect. C,* **2015**, *71* (1), 3-8.
[6]. Patil, P. H.; Filonenko, G. A.; Lapointe, S.; Fayzullin, R. R.; Khusnutdinova, J. R., Interplay between the Conformational Flexibility and Photoluminescent Properties of Mononuclear Pyridinophanecopper(I) Complexes. *Inorg. Chem.,* **2018**, *57* (16), 10009-10027.
[7]. Costentin, C.; Drouet, S.; Robert, M.; Savéant, J.-M., Turnover Numbers, Turnover Frequencies, and Overpotential in Molecular Catalysis of Electrochemical Reactions. Cyclic Voltammetry and Preparative-Scale Electrolysis. *J. Am. Chem. Soc.,* **2012**, *134* (27), 11235-11242.
[8]. Costentin, C.; Savéant, J.-M., Multielectron, Multistep Molecular Catalysis of Electrochemical Reactions: Benchmarking of Homogeneous Catalysts. *ChemElectroChem,* **2014**, *1* (7), 1226-1236.
[9]. Wasylenko, D. J.; Rodríguez, C.; Pegis, M. L.; Mayer, J. M., Direct Comparison of Electrochemical and Spectrochemical Kinetics for Catalytic Oxygen Reduction. *J. Am. Chem. Soc.,* **2014**, *136* (36), 12544-12547.
[10]. Matheu, R.; Neudeck, S.; Meyer, F.; Sala, X.; Llobet, A., Foot of the Wave Analysis for Mechanistic Elucidation and Benchmarking Applications in Molecular Water Oxidation Catalysis. *ChemSusChem,* **2016**, *9* (23), 3361-3369.
[11]. Langerman, M.; Hetterscheid, D. G. H., Fast Oxygen Reduction Catalyzed by a Copper(II) Tris(2-pyridylmethyl)amine Complex through a Stepwise Mechanism. *Angew. Chem. Int. Ed.,* **2019**, *58* (37), 12974-12978.
[12]. Zhang, H.-T.; Xie, F.; Guo, Y.-H.; Xiao, Y.; Zhang, M.-T., Selective Four-Electron Reduction of Oxygen by a Nonheme Heterobimetallic CuFe Complex. *Angew. Chem. Int. Ed.,* **2023**, *62* (48), e202310775.
[13]. Fukuzumi, S.; Tahsini, L.; Lee, Y.-M.; Ohkubo, K.; Nam, W.; Karlin, K. D., Factors That Control Catalytic Two-versus Four-Electron Reduction of Dioxygen by Copper Complexes. *J. Am. Chem. Soc.,* **2012**, *134* (16), 7025-7035.
[14]. Kakuda, S.; Peterson, R. L.; Ohkubo, K.; Karlin, K. D.; Fukuzumi, S., Enhanced Catalytic Four-Electron Dioxygen (O2) and Two-Electron Hydrogen Peroxide (H2O2) Reduction with a Copper(II) Complex Possessing a Pendant Ligand Pivalamido Group. *J. Am. Chem. Soc.,* **2013**, *135* (17), 6513-6522.
[15]. Wang, Y.-H.; Pegis, M. L.; Mayer, J. M.; Stahl, S. S., Molecular Cobalt Catalysts for O2 Reduction: Low-Overpotential Production of H2O2 and Comparison with Iron-Based Catalysts. *J. Am. Chem. Soc.,* **2017**, *139* (46), 16458-16461.
[16]. Pegis, M. L.; Martin, D. J.; Wise, C. F.; Brezny, A. C.; Johnson, S. I.; Johnson, L. E.; Kumar, N.; Raugei, S.; Mayer, J. M., Mechanism of Catalytic O2 Reduction by Iron Tetraphenylporphyrin. *J. Am. Chem. Soc.,* **2019**, *141* (20), 8315-8326.